ingegneria sismica
International Journal of Earthquake Engineering
Anno XLIII - Num. 2 - 2026

Design of an Intelligent Analysis System for the Structural Evolution of Alkali-Treated Euglena Polysaccharides via Multimodal Data Fusion

Yingtong Sui[1] *Mingyi Shen*[1], *Ruifang Wang*[1], *Zhengbiao Gu*[1,2,3,4], *Yan·Hong*[1,2,3,4], *Zhaofeng Li*[1,2,3,4], *Caiming Li*[1,2,3,4], *Xiaofeng Ban*[1,2,3,4], *Lingjin Li*[1,2,3,4], *Danyang Li*[1,2,3,4] *and Li Cheng*[1,2,3,4,*]

[1] School of Food Science and Technology, Jiangnan University, Wuxi 214122, China
[2] State Key Laboratory of Food Science and Technology, Jiangnan University, Wuxi 214122, China
[3] Collaborative Innovation Center of Food Safety and Quality Control in Jiangsu Province, Jiangnan University, Wuxi 214122, China
[4] National Engineering Research Center for Functional Food, Jiangnan University, Wuxi 214122, China

SUMMARY: *Alkali treatment is an effective method to separate and activate Euglenoid-derived paramylon; However, it may alter other properties such as molecular Size, Crystallinity Packing, Hydrogen-Bond Network, and Conformation of Beta-1,3-glucan backbones. Developed and validated a smart analysis System to track the Structural Evolution of alkali-treated Euglena polysaccharide based on empirical multi-modal characterisation Data. Paramylon-rich polysaccharides were treated with NaOH at 0.1, 0.3, 0.5, 0.7, and 0.9 mol L-1At 45 degrees Celsius for 2, 6, and 12 hours; the untreated groups were set as control. Produced 192 records from four biological extraction batches, each with three replicate analyses. Each entry included FT-IR spectrum, NMR-informed linkages, SEC-MALS molecular-weight values, XRD crystallinity coefficients, Congo-red conformer assessments, as well as particle morphology parameters. A modality-aware fusion model was trained to predict weight-average molecular weight, a composite structural-integrity index, trihelices retention, Beta-1,3 linkages retention and four different Structural States. Empirical data present a series of alkali-responsiveness stages. The structural stability was reduced by 42% and reached 83.8% after being added with 0.1mol/L, respectively.-1for 2 h, 0.626 at 0.5 mol L-1for 6 h, and 0.354 at 0.9 mol L-1For 12 hours. The corresponding MW values decreased as follows: 356 kDa → 331; 204 kDa; 82 kDa, triple-helix retention decreased from 100% to 91.2%; 67.2%; 39.4%. The proposed fusion method obtained an Mw RMSE of 8.9 kDa, an S_int RMSE of 0.024, a macro-F1 of 0.942, an AUROC of 0.985, and an expected calibration error of 0.031 compared with the FTIR-alone, NMR-alone, SEC-XRD alone or morphology-only early-fusion baselines. Ablated experiments confirmed that cross-modal attention, treatment embedding, structural-consistency loss, missing-modality masking, and calibration all contributed individually to the final results. The system maps the heterogeneous experimental results to a state-aware structure-evolution diagram and can perform batch screening, confirmatory measurement selection, and interpretability assessment of alkali-treatment degree. The figure sequence organisation structure is not empirical evidence but empirical supplements; Descriptors curves, three-dimensional structured landscapes, Latent state topologies, prediction performances, ablative behaviours, calibration methods, error distributions, case-level interpretations are presented separately. The moderate treatment zone has shown greater ambiguity; crystallinity*

*chenglichocolate@163.com
https://doi.org/10.65102/is2026782
Published: 30 April, 2026

and conformations decreased before molecular size collapse was complete. Calibrated fusion output, which includes both the state labels and the verification indications. Therefore, it can be connected with confirmation experiments of SEC-MALs, XRD, Congo-red and NMR techniques when the sample is close to the swelling-transition interface.

KEYWORDS: *Euglena polysaccharide; Paramylon; alkali treatment; multimodal data fusion; Structural evolution.*

1 Introduction

Paramylon-rich Euglena polysaccharide has moved from the lab to function in foods, feeds, medicine and Biorefineries, etc. These Applications cannot judge product quality solely based on the Recovery Yield. A batch is mass-balanced but loses molecular weight, crystal structure or conformation after the processes of extraction and processing. Pilot-scale paramylon extraction has already demonstrated high-purity products and processes with good scaleability; new solvent systems also show increased recoveries in the market [1-3]. In order to solve the following generation control problem: by improving extraction techniques or alkoxygen-borne methods in beta-glucoside purification for subsequent separation and removal from solutions; Then Further development will also need Transformation Technologies To Achieve This Purpose.

Alkaline-processed Euglenophyta polysaccharides need to be compared in multiple biological batches. Cultivation Mode, Harvest Stage and Cell Disruption History can change the granular accessability and Alkaline Response under the same NaOH Concentration and Exposure Time. A model without considering this record-level variation is prone to learning an overall severity curve and missing boundary samples. Therefore, in this study, each measurement is considered an individual recorded sample with specific content: the treatment conditions, batches, analytical repetitions, descriptors' uncertainly information, modes of availability;

The raw materials also add to it. High-throughput screening of paramylon-rich Euglena mutant strains to explore metabolic mechanisms and industrialisation pathways for increasing β-1,3-glucan contents [4]. These Routes produce materials Streams with diverse cell history and particle characteristic values. The structural investigation of Euglenopolysaccharides shows that the compositions, Linkages or other factors can affect their biological and physical properties [5, 6]. For alkaline processing, yield and purity therefore cannot determine whether the treated product remains suitable for functional use. The analysis system should determine where each of the samples falls on this preservation-swelling-transformation-depolymerisation route.

Routine Characterisation provides further assistance for this study. FTIR spectra report glycosidic-bond fingerprints, hydroxyl environments, and local chemical changes, and are widely used in polysaccharide structural analysis [7]. NMR-derived features show greater link-layer confirmation when there is enough sample quantity and instrument-time coverage. SEC-MALS quantifies Molecular-Weight Distribution and Polydispersity. XRD records crystalline Packing. Congo-red assays indicate triple-helix-related conformation. Micrometer: Granule swelling, surface damage and fragmentation visible. These forms include the corresponding structures at various levels of response to alkali in different rates, making it impossible for side-by-side report conversion into process decisions.

Paramylon's crystalline β-1,3-glucan granular form is suitable for chemical determinations. molecular-size factors indicate chain-loss lengths. FT-IR ratio displays fingerprint and water-related changes. XRD shows ordered packing. Congo-red Response indicates conformational

retention. NMR-informed descriptors support linkage preservation and local carbon-environment assessment. Microscopic records particle-scale swelling and rupture. Slightly, X-ray diffraction (XRD) peaks may be wide or the form changed without substantial change in links. A severe state will decrease the molecular weight, weaken the linkagesignal, and move all modes towards depolymerisation simultaneously.

The multi-layered response is why a simple ratio Table, Mw value, crystallinity index, and microstructure analysis cannot fully represent it. Middle-exposure Zone has a relatively unstable situation. If crystallinity decreases while Mw is still moderate, the material might be considered a swelling products or an early degraded form under certain linkage remaining and conformative conditions. Therefore, the decision need to be established prior to model construction. The research subject in this study is a record-level structured State with an uncertain output of continuous descriptor target information.

Multimodal fusion can be applied to these chemical levels only. Low-level concatenation treats all descriptor blocks as having equal availability and information content; it cannot distinguish between polysaccharides well. Security MALS is more successful in identifying depolymerisation. XRD and Congo-red have higher information in the swelled and transition zones. FTIR supports rapid screening but cannot resolve molecular-weight distribution. Morphology improves physical interpretation but cannot confirm backbone preservation alone. The proposed system separates modal tokenisations before cross-modal interaction; The predicted results indicate which pieces of evidence block contributed to each state.

Alkali treatment introduces staged responses of the structure. Early indication includes edema, matrix relaxation and hydrogen bonds reformation without immediate core rupture. Moderate exposure reduces crystallinity and changes conformations, but recognisable β-glucan spectral characteristics are still retained. Major damage will reduce losses of part of the connections. Studies on alkali-extractable or alkali-treated polysaccharides have shown changes in molecular weight, viscosity, crystallinity and the chemical Environment; The size of their responses varies among different polymers sources, strengths and detection methods. [8-10] The crystal-granular structure of Euglena paramylon enhances the complexity and thus requires state identification to rely jointly on multiple pieces of evidence rather than one peak value, ratio, or chromatographic indicator.

Fusion of data can be used to handle the above-mentioned evidence form. Heterogeneous modalities have shown significant improvement in spectral and sensor fusion for food and chemical analysis due to their complementary information during this process [11, 12]. Supervised fusion has also demonstrated superiority over simple concatenation in supervised-fusion-based real-world spectroscopic regression problems with small samples and varying information content across different data sources [13]. Multimodal fusion has been extended to quality and safety evaluation, and cross-fusion networks have also been employed in paired vibrational-spectroscopy data, including Raman and FT-IR. Although these methods may apply in this context; However, the adaptation of them to alkali-treated Euglena polysaccharide is not intended for general use.

There are missing modality parts in the experiment. The laboratory can measure FTIR for each aliquot and reserve NMR, SEC-MALS or high-resolution microscopy for particular samples due to their associated costs, requirements by samples, etc. Impute missing Descriptors without taking a mask; thus, the model might misinterpret instrumental absence as chemical data. Therefore, the current system has recorded the issue of missing data during analysis. The modality mask enters the model through descriptions and affects uncertainty prediction; It is required in a stage of characterisation that low-cost screening identifies candidates for further verification.

Ask whether heterogeneous measurements of alkali-treatment-Euglena polysaccharides

could be calibrated to produce a structured-structural Evolution Map that delineates the four types: native-like, swollen, transition, and depolymerised. The analysis needs to present three types of evidence: a plausible distribution map corresponding to a reasonable concentration-time response; A combined model outperformed multiple base lines in held-out validation tests; And an explanation mechanism showed which aspects affected the outcome through uncertain information, missing data or specific cases.

Three kinds of deficiencies appear. Many of the treatment studies report instrumental outcomes next to corresponding record-level structural-state decisions in non-convertible form. Secondly, treatment variables are often treated as metadata; meanwhile, concentrations, times, and temperatures form an exposed area to generate structures Changes. Thirdly, the real characterisation campaign is not perfect; IR+logs are commonly used, but SEC-MALs, NMR, etc., high-quality morphological analysis methods may be unselected. Therefore, a helpful analysis system should have records combining exposure factors with multi-modal features and modality labels.

Aim to Establish an Empirical Multimodal Analysis System of Alkali-reated Euglena Polysaccharides. Paramylon-rich samples were subjected to controlled NaOH concentrations-times matrices and characterised by means of FT-IR, NMR-based linkages descriptor, SEC-MALS, XRD, Congo-red conformation analyses and particle morphologies. Organised in terms of record-level multi-modal observation data. A fused model that predicted continuous structural features and categorised each instance as either native-like, swollen, transitional or depolymerized state. The work provides a measured descriptor map, a modality-aware fusion model with calibration and missing-modality handling, and figure-level evidence for descriptor evolution, three-dimensional state topology, prediction accuracy, robustness, and representative case interpretation. Its conclusions are based on the tested Eugeniaa materials, alkaline methods and confirmed data sets, thresholds must be recalculated under diverse Strain extraction routes and product standards.

2 Methods

2.1 Alkali treatment experiment, multimodal characterization, and record construction

The experimental subject was a paramylon-rich polysaccharide fraction extracted from heterotrophically-cultivated Euglena gracilis biomass. After washing the fraction repeatedly to remove all traces of pigment in the supernatant, it was dried at 45°C under a vacuum. Before alkali treatment, check using FT-IR and XRD that there are β-glucan fingerprint bands in the original material and its crystalline diffraction pattern has been established. The original control was not in contact with sodium hydroxide and followed the same neutralisation, washes and drys as those conducted on the treated samples. The control that served as the benchmark in terms of structural integrity normalisation and retained value calculations.

The alkali-treatment matrix used five NaOH concentrations, 0.1, 0.3, 0.5, 0.7, and 0.9 mol L-1, and three exposure times, 2, 6, and 12 h. Set treatment temperature at 45°C for separating the concentration-Time effect. Dissolve each condition's 200mg dry polysaccharide with 20 mL NaOH solution under gentle stirring at a speed of 300 r/min. Immediately cooled and adjusted the acidity to pH 7.0 using dilute hydrochloric acid. Washing the materials with deionised water to a conductance of less than 20μScm-1 and then freeze-dried after that. Four different extraction batches were carried out separately, and each batch was reanalyzed three times. There were a total of 192 samples in the final records, including 16 different treatments, 4 biological batches and 3 duplicate analyses.

Alkaline treatment before exposure: A paramylon-rich fraction was suspended in deionised water under controlled stirring conditions to reduce local concentrations. The solid-lquid ratio was set uniformly for all groups to isolate differences in descriptor change solely on the basis of varying degree of contamination. NaOH Treatment, and then make it neutralised at a pH of 7·0; Wash until the conductivity stabilised before freezing dried using the same drying programme. The untreated control passed through the same washing and drying process but added no sodium hydroxide; therefore, retention descriptors could be evaluated relative to a processed reference rather than that of the original dry matter.

Instrumental acquisition is used to maintain a connection between the actual aliquot and the corresponding model record. Each treated batch was divided into matched aliquots for FTIR, SEC-MSA, XRD, Congo-red, NMR-guided analyses, etc. FT-IR spectrum for each sample presented here. SEC-MALS and XRD/Congo-red were measured for each condition-batch combination; NMR-informed descriptors were given replicate uncertainties due to the need for high sample masses in linkage-level acquisitions and additional instrument times. Field microscopes were taken at independently scattered particles to aggregate the particle descriptors under the conditions-batches levels before record construction.

Table 1 shows the experimental data structure. The FT-IR spectrum was obtained for all of the 192 samples to serve as a general screening method. SEC-MALS, XRD, Congo-red, and NMR-informed descriptors were obtained from batch-level aliquots, producing complete values for condition-batch records and repeated assignment to analytical replicates with replicate-level uncertainty tags. Based on at least 600 particles for all treatments under different conditions, calculate the morphological feature values. This organisation corresponds to the real Laboratory workflow: rapid spectrum acquisition is dense; High-specificity structural analysis has lower density and a higher cost. Therefore, it has received the modality mask instead of a presumed entire feature vector.

Table 1: Experiential Design and multi-modal Data Acquisition.

Experimental block	Levels or count	Role in empirical dataset
Treatment matrix	NaOH 0.1-0.9 mol L^{-1}; 2, 6, 12 h; 45 °C	Defines alkali exposure field
Native control	Untreated material, four batches, three replicates	Reference for retention descriptors
Record number	192 sample-level records	Model input and validation unit
FTIR	192 spectra, 1800-850 cm^-1	Routine chemical fingerprint
NMR-informed descriptors	Condition-batch aliquots with replicate uncertainty tag	Linkage and local chemical-environment evidence
SEC-MALS	Condition-batch aliquots	Mw, Mn, PDI, high-Mw fraction
XRD/Congo red	Condition-batch aliquots	Crystallinity and triple-helix-related conformation
Morphology	≥600 segmented particles per condition	Swelling, roughness, fragmentation

Preprocess FTIR spectra before training by removing the 1800-850 cm^{-1} fingerprint area, as well as performing asymmetric least-squares baseline correction, Savitzky-Golay smoothing, and vector normalisation. Using the ratios of 1155/1030 and 897/1030 cm^{-1} to represent β-glucan fingerprints; Retained 1640/1030 cm^{-1} as a hydration and disorder indicator. The whole normalised spectrum, which includes the full range of hydrogen bond variations. Sec-MALS chromatogram data with unstable baseline signals, injected peak abnormalities or incomplete elution were eliminated; Mw,Mn,PDI,and high-molecular-weight fraction components were

separated, and log-scale molecular weights as input data was stable trained. XRD crystallinity, peak broadening, peak shifts, Congo-red red-shift, and helix-retention ratio formed the supramolecular descriptor block. Structural labels were assigned from measured descriptors rather than treatment conditions: native-like, swelling, transition, and depolymerized states were defined by molecular-weight retention, crystallinity, β-glucan bands, conformation evidence, and integrity index.

After collecting all the modal parameters, a combined structure-entirely integrity Index was constructed. Using a specific formula in regression and performing state estimation; However, this does not substitute for the original descriptors directly.

$$S_i = w_1 R_{Mw,i} + w_2 R_{\beta,i} + w_3 R_{H,i} + w_4 R_{X,i} + w_5 R_{M,i}, \quad \sum_{k=1}^{5} w_k = 1 \tag{1}$$

S_i is the structure and integrity assessment index for record i. $R_{Mw,i}$ Molecular-weight retention by SEC-MALS; $R_{\beta,i}$: Retention time of β-1,3 linkage from NMR-informed descriptors; $R_{H,i}$: Triple-helix ratio by Congo-red analysis; $R_{X,i}$: Crystallinity degree by XRD; $R_{M,i}$: Morphological integrity index calculated as the product of particle compactness and fragment fractions. Weights $w_1 \sim w_5$ were selected as 0.30, 0.22, 0.20, 0.18 and 0.10 respectively after a sensitivity test was performed. Given that molecular size received the highest weight due to its greater influence on chain scission as an immediate response to alkali corrosion; and morphological changes were deemed less significant in comparison, thereby reducing their weights accordingly.

Extracted morphology descriptors of segmented granule images after removing obvious dust, fusing aggregates that could not be separated, and discarding out-of-focus particles. Calculate the median diameter, interquartile range, circularity factor, roughness value, fragment fraction among all conditions. Using the median instead of the mean increased resistance to a small quantity of broken particles. Morphological evidence was not considered definitive confirmation of depolymerisation. Used to identify swollen areas, surface damage, and fragmentary changes in the interpretation of spectral and molecular-size evidences.

Structural-State labels were given after extracting descriptors, not directly based on the NaOH concentration. So as not to learn a treatment shortcut in this way. A sample subject to a nominally weak circumstance may, according to SEC-MALS and conformation evidence, be designated as a transition case. A moderate condition would still be classified as swollen even with weak linkage retention and a large-sized drug molecule. Two analysts reviewed the labels of the descriptors that were not in the model split. Borderline cases were not mentioned until all the descriptors had been determined; therefore, they could not be adapted to match the labels easily.

Table 2 shows the feature Blocks and their structures. The Table below serves as a reference to build charts and models. Each descriptor was normalised in the modality of its training set. Normalized the FT-IR vector to eliminate sample-load-related interference. SEC-MALS variables were log-transformed when right-skewed. XRD and Congo-red descriptors were normalised to the native control. Summary morphology descriptors by median and interquartile range to reduce the impact of segmented outlier data. No missing data were filled with zeros. A binary availability mask indicated whether the value had been measured (interpolated) from a condition-batch aliquot, or absent.

Table 2: Features Blocks Used in Multimodal Structural-Evolution Analysis.

Feature block	Representative descriptors	Unit or scale	Structural meaning
FTIR	Normalized fingerprint vector; 1155/1030, 897/1030, 1640/1030 ratios	a.u.; ratio	Glycosidic fingerprint and local chemical environment
NMR-informed	beta-1,3 retention; C1/C3 stability; carbonyl-related signal	% or normalized score	Backbone/linkage preservation
SEC-MALS	Mw, Mn, PDI, hydrodynamic-radius proxy, high-Mw fraction	kDa; ratio	Chain-size distribution and depolymerization
XRD	Crystallinity index, peak width, peak shift	%; degree	Ordered packing and crystalline domain loss
Congo red	Maximum red-shift; helix-retention ratio	nm; %	Triple-helix-related conformation
Morphology	Median diameter, circularity, roughness, fragment fraction	μm; ratio	Granule swelling and physical fragmentation
Treatment	Concentration, time, temperature, concentration-time product	mol L^{-1}; h; °C	Exposure context driving structural change

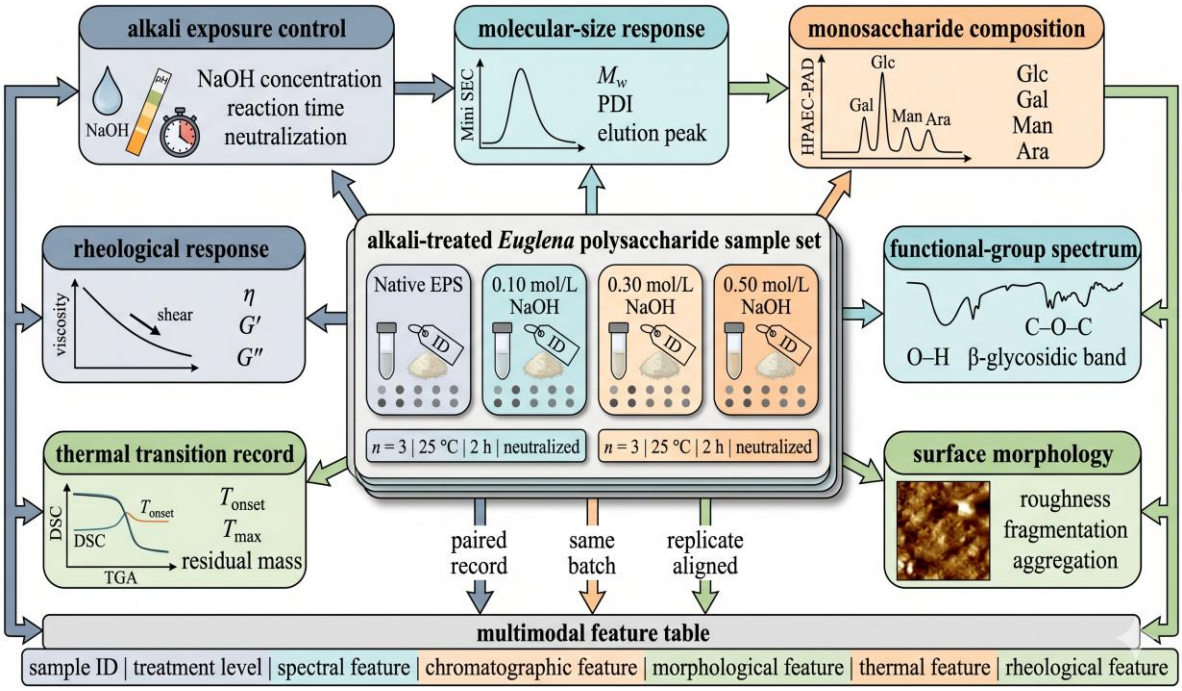

Figure 1: Experiential multimodal recording establishment of alkali-treated Euglena polysaccharides.

2.2 Multimodal fusion model and chemically constrained inference

The model inputs a total of six parts: FTIR, NMR-informed bond-descriptor; SEC-MLASXRD/Congo-red conformer; morphology, etc.; And the treatment variable. Each block is encoded in modalitiespecific encoder to prevent the forced reduction of descriptor scales

prior to representation learning. Dense chemical descriptors use two-layer feed-forward encoders with layer normalization. A shallow one-dimensional convolutional encoder is adopted immediately after global average pooling to retain some local bandshape information and reduce the size of the feature map. Treatment variable encoding: concentration × 1, Time × T, Temperature \times Temp, Concentration×Time×Product , temperature-weighted Severity. The availability mask is added to the encoded modalities token, and then it impacts uncertainly prediction.

Compact one-dimensional convolutional structures based on FTIR encoders were selected to capture local bandwidth differences; The parameters of these Structures are compatible with those of the Sample data. Descriptor encoders for NMR-influenced, SEC-MALS, XRD/Congo-red, morphology and treatment variables used a small multi-layer perceptron with layer normalisation. Each encoder produced the same dimension modality token that was compared within a shared latent space without constraining raw variables to have equal scale or distribution.

The treatment embedding was presented as the alkali severity causal-exposure area. Concentration, exposure time, Temperature and concentration-times products were included. Temperature has been maintained in the primary matrix because there may be other gradient temperature-experiment designs without altering the database structure. This embedding does not replace measured evidence; it helps distinguish those with relatively similar FT-IR spectra but different exposure histories and unknown molecular-size degradation.

A modalitymask was added to each token before the attention mechanism. Empty measurement areas were replaced by neutral fillers and marked as unavailable in the mask. Therefore, the model could be designed to consider that lack of SEC-MALS data would reduce uncertainty in such samples but not miss some effects from missing morphology data; This setting represents the regular empirical deployment; thus, incomplete characterisation often occurs.

Only a few heads were used in the cross-modal attention layer due to a relatively low number of modalities and chemical structure. To simulate the interaction of evidence among FTIR-SEC-MALs, conformations-morphologies-treatment states; it is not intended for optimisation of representation capabilities. Attention Weights were exported as diagnostic evidence rather than causal proof. Depolymerisation prediction generally needs to include the SEP-MAL signal; If the case is predominantly morphology but with contradictory molecular weight, it must be reviewed by experts first. The fused processing function is shown below:

$$\mathbf{z}_i = \sum_{m=1}^{M} \alpha_{i,m}\, \mathbf{h}_{i,m}, \quad \alpha_{i,m} = \frac{exp(q_i^{\top} k_{i,m})}{\sum_{r=1}^{M} exp(q_i^{\top} k_{i,r})} \tag{2}$$

$\mathbf{z}_i$ in this case denotes a merged latent feature of record i. $\mathbf{h}_{i,m}$ is the token-encoded representation of modality m. $\alpha_{i,m}$ is the attention weight given to modality m. q_i is the query vector obtained from the treatment-aware record representation; It is a key vector corresponding to modality m; d indicates the hidden dimension; And M represents the number of available modalities. The mask removes unavailable modalities from the attention denominator. To prevent the model from learning an artificial relationship between missing data and features.

$Mw\beta Mw$The output Head outputs five consecutive targets and one class label. Continuously monitor the following indicators: Mw, S_i; triple-helix retention; β-1; 3-Linkage retention; crystalline retention. Categorisation of heads that predict native, swollen, transitional or depolymerised states. multitask learning was chosen due to chemical linkages among the outputs. The predicted result of both high integrity and low Mw should be considered unsatisfactory, except when the descriptor evidence shows a reasonable exception. A structural consistency penalty can be used to prevent predicted integrity (predictedI), linkage retention

(linker_retention) and molecular-size correction retained data drift under the same treatment level; As a goal of the training work.

$$L=\lambda_1 MSE(\hat{\mathbf{y}}_i,\mathbf{y}_i)+\lambda_2 CE(\hat{\mathbf{p}}_i,s_i)+\lambda_3\Omega_{chem}+\lambda_4\Omega_{cal} \quad (3)$$

L is the comprehensive optimisation goal here. MSE compares the predicted continuous vector $\hat{\mathbf{y}}_i$ and the measured target vector $\mathbf{y}_i$. CE compares the predicted state-likelihood vector $\hat{\mathbf{p}}_i$ and assigns a particular class c_i. λ_1 to λ_4 were assigned a value of 1.0, 0.8, 0.3, and 0.1 following cross-validation optimisation. The consistency term was treated as a weak penalty; since the alkali-reaction function is not monotonically related to all descriptors. This prevents uncontrolled swelling and descriptors' offset errors, as well as chemical non-realistic interactions.

A continuous output head predicts *Mw*, S_{int}, triple-helix retention, β-1,3 linkage retention and crystallinity; A classification head predicts four structural states. Both of them were together trained; that is, they have been given the same structures as well. Reducing inconsistent Outputs, such as a combination of high depolymerisation probability and high Integrity or low Molecular-Weight retention; to enhance the Consistency of process-level decisions.

A structural-constancy loss penalty for chemically invalid combination while not requiring a monotonous response of each treatment condition. It focused on local defects such as: over-estimated prediction accuracy, high Sint value, low β-1,3 content of supports; Unsupported severity reversal phenomena. Therefore, local nonlinear responses were preserved but chemically inconsistent output packets were suppressed.

Due to using state probabilities in the routing process; because temperature scaling was trained on the validation dataset and then applied to holdout test data. The model presented the most likely state and confidence level. Low-confidence traces and those marked as having high modality uncertainty were referred to confirmation tests; thus, it served instead of just being an automated hard-labelling system.

The hyperparameters were chosen from the pre-defined grids for token dimension, attention heads, dropout, learning rates, and the weights of consistency and calibration terms. The chosen model has a minimum overall validation error, while also being well-calibrated; The evaluation of the test set followed the protocol used in evaluating all baselines.

Training used Adam [19], batch size 24, early stopping on validation macro-F1 and Si RMSE, and a maximum of 300 epochs. The learning rate started at 1.0 × 10-3 and was halved after 20 epochs without validation-loss improvement. Token dropout was 0.15, and random modality dropout improved tolerance to incomplete characterization. The SHAP-style attribution provided case-level interpretation, but only used the umap method to inspect the training topology;

Place Figure 2 after the loss function definition, respectively. It should show a closed mechanism layout with a central latent structural state, surrounding modality encoders, treatment embedding, consistency constraint, uncertainty output, and state/descriptor heads, highlighting modality-specific encoding, masked cross-modal attention, structural-consistency loss, and calibrated output.

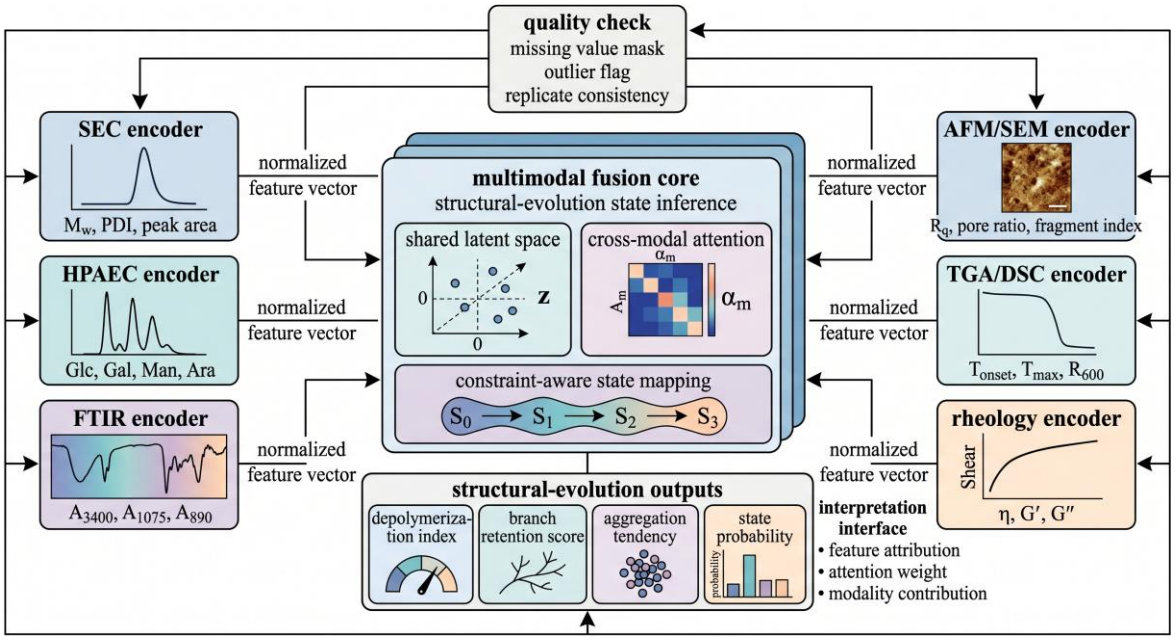

Figure 2: Modality-aware structure-variation recognition algorithm.

2.3 Evaluation protocol, statistical analysis, and deployment interface

Design the assessment plan to check if the learning of this system exhibits structural-principle relationships rather than simple recollections about treatment scenarios. Records are divided into conditions-batch groups to avoid analysing replicates from the same condition in both training and testing datasets at once. The primary division employed a ratio of 70:30-40 among the condition-BATCH groups in its train-validate-test distribution plan. Five times repeated the condition-held-out test for verification of stability. Only after scaling on the training set did these data points apply across the validation and testing sets. There is no data corresponding to the test condition in feature scaling, temperature calibration, UMAP projection fit and threshold selection.

Split randomly according to the treatment condition at all times possible, not each replicate. It has a more rigorous specification than randomised record-splitting, testing whether the model generalises to the concentration-time domain rather than being trained on replicate-specific regularities. Replicate from the same condition and place them together at different splits. Scaling statistics, PCA check and UMAP fit were obtained from the training set and then used for validations and tests. Hence, there was no inclusion of out-of-sample data in the pre-processing stage.

Base model training used the same responses for both training sets. FTIR-only models received the normalized spectra and FTIR ratios. NMR-based model links to and local chemical-environment descriptor. SEC-XRD models obtained molecular-scale and ordered/unchained attributes. Morphology-only models obtained particle statistics. Early fusion received all normalized descriptors in one concatenated vector. The selection of this kind is conservative, so all baselines have used the best set of data in each case; The combination process of the model will also be compared with that of other models.

Compared to five reference models: FTIR-only convolutions/Classification; NMR-influenced Random Forests; SEM-XRD partial Least Squares + Classifier Head, Morphology-only Random Forests and Early Fusion of Concatenated Normalised Descriptors. The baseline was taken as the normal laboratory choice. FTIR-only reflects rapid screening. NMR-informed and SEC-XRD baselines reflect high-specificity but narrower characterization. Only

morphology determines the appearance of particles sufficient to determine states. Early fused tests if simple concatenation of all descriptors can work well initially. The evaluation of this model under the same train-validation-test split used by each baseline.

Regression performance was reported by RMSE and mean absolute error. Macro-1F1, balanced accuracy, and AUC-ROC were reported for classification. Calibration has an expected calibration error and a reliable curve. The test of missing-modalities is a systematic way to mask one modality in the output during training and screen with reduced input combinations. Cases were taken of native, mild, moderate and severely alkaline areas respectively for interpretation. Mean value±S.D. was used to express the results of biological batches in statistics. The difference in model settings was verified through paired comparisons after splitting repeatedly; In practice, if the error is less than that of adjacent structures, it is considered relevant to reality.

The metric definitions shown in the tables and figures were as follows.

$$RMSE=\sqrt{\frac{1}{N}\sum_{i=1}^{N}(\hat{y}_i-y_i)^2},\quad ECE=\sum_{b=1}^{B}\frac{|I_b|}{N}|acc(I_b)-conf(I_b)| \tag{4}$$

RMSE stands for the root mean square error of a continuous objective function y_i; $\hat{y}_i$ corresponds to prediction on a particular data point i. N is the total number of evaluations. MacroF1 refers to the unweighted average of each class's F1 score across K structures. Precision and recall of the states k P_k and R_k, respectively. MACRO-F1 was selected as the primary evaluation indicator since it is relatively easier to categorise swelling and transformation data compared with that of original-state and depolymerised State; Overall accuracy masks such boundaries' errors.

Ablation test excluded each part separately: removal of the treatment embedding, cross-modal attention, structural-consistency loss, modality mask, and calibration. The no-treatment setting excluded concentration, time, temperature, and concentration-time product; no-attention replaced attention with average pooling; no-consistency removed the chemical-coherence penalty; no-mask removed modality-availability indicators; and no-calibration used raw softmax probabilities. Each result in Figure 8 therefore corresponds to a defined model component.

Missing-modality tests removed one or more of the measurement blocks during testing, without altering the trained model and calibration parameters. Macro-1, SINT RMSE and Mean Predictive Uncertainty are given. The performance decline and widened uncertainties indicated that whether the model could process missing SEC-MALS or XRD/Congo-red data, as well as route indeterminate cases for further verification.

At the case-level interpretation of four records each type: original; mild; medium; Severe. Each report included an FTIR fingerprint curve, normalised descriptor Radar value, state probability and modality evidence weight. Excluded from the model-building process and used exclusively as references for comparing predicted state with chemicals or physics tests data.

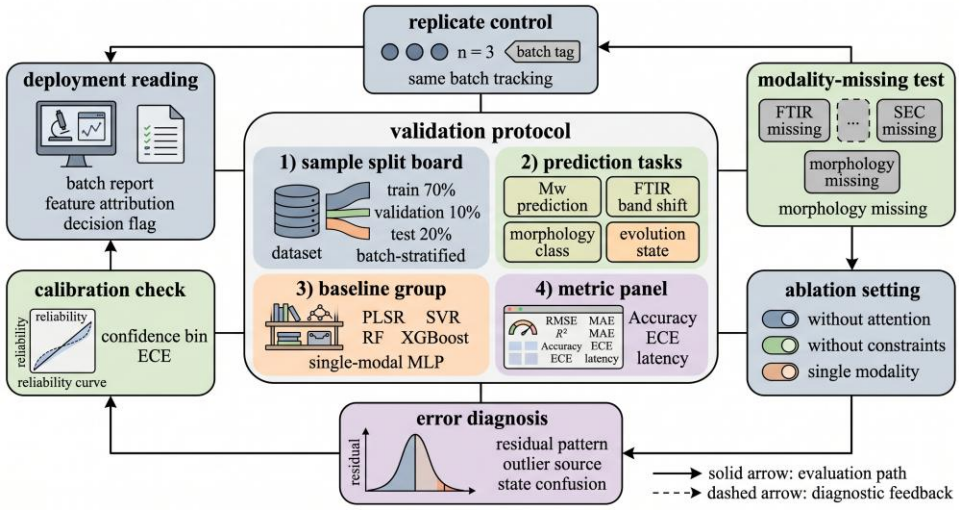

Figure 3: Evaluative Plan of Empirical Multimodal Fusion and Structural-State Verification.

3 Results and Discussion

3.1 Empirical descriptor evolution under alkali treatment

The first results section will determine if an alkali-matrix-generated chemical structure evolution has been interpretable. The multimodal descriptor varied with concentration and time, but it did not change at the same speed. As shown in this paper's main purpose and reason for the system requiring multimodal fusion; As shown in Fig. 4, the treatment-driven evolution of modal structural descriptions.

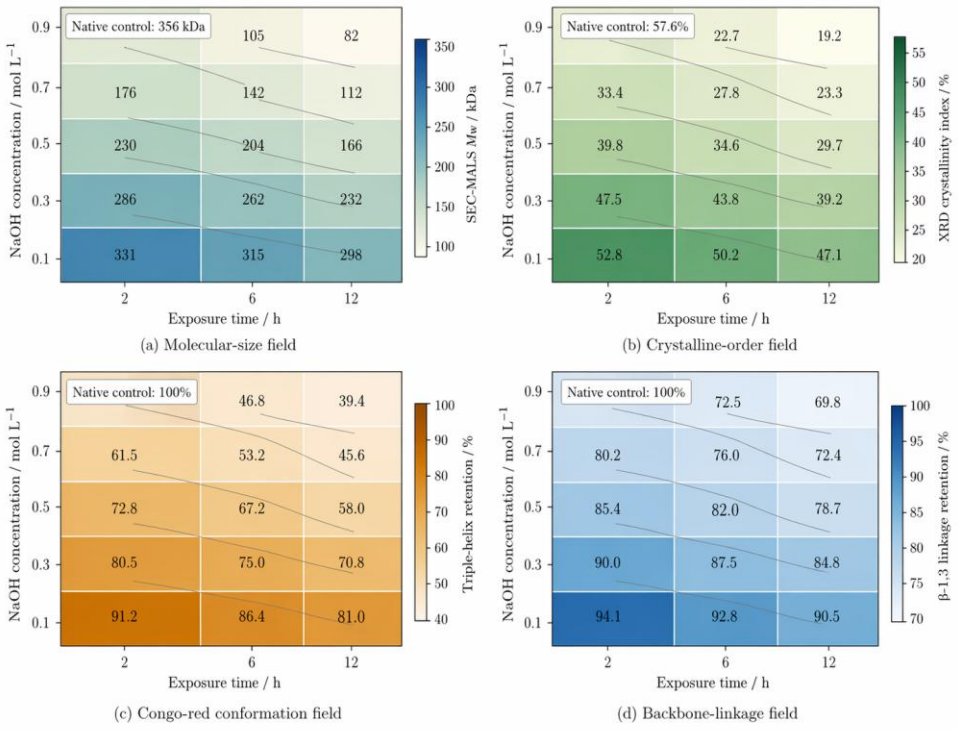

Figure 4. Multimodal structural evidence of alkali-treatment of Euglena polysaccharides.

Figure 4(a) presents a stepwise reduction in Mw at the alkali site. The MW of Mw decreased from 356 kDa in the wild type control to 331 kDa after incubation for 0.1 mol·L^-1 pH range from 0.1 to 0.9 h, then increased by a factor of about three under other conditions. When NaOH concentration exceeded 0.5 mol/L, or if the exposure time was more than 12 hours; The most serious decrease occurred for both swellability and packaginess.

Figure 4(b) shows earlier loss of crystalline order. Crystal index After exposure to normal treatment Conditions, respectively 57.6% 34.6 per centand 19.2%. At 0.3 mol L-1 for 6 h, Mw remained 262 kDa, whereas crystallinity had already fallen to 43.8%, showing that supramolecular packing weakened before severe molecular-size loss.

Figure 4(c) shows that triple-helix retention followed crystallinity more closely than Mw. It decreased from 100% in the native control to 91.2%, 67.2%, and 39.4% under 0.1 mol L-1 for 2 h, 0.5 mol L-1 for 6 h, and 0.9 mol L^-1 for 12 h. Therefore, moderate samples had a measurable molecular size but lacked the native-like conformation.

Figure 4(d) shows that β-1,3 linkage retention declined later than conformation. At 0.1 M/L, it was 94.1%, at 0.3 M/L for 6 hours, which was 87.5%; Then fell to 69.8% within 12 hours of being added at a concentration of 0.9 M/L. The lagging decline divides controlled swelling from backbone-level damage, and none of the descriptors can fully represent the situation of treatment change.

There were significant differences under medium alkaline Conditions. At 0.3 mol L-1 for 6 h, Mw remained 262 kDa, but crystallinity and helix retention had fallen to 43.8% and 78.4%, indicating a swelling state with altered granule organization and preserved backbone evidence. At 0.5 M for 6 hours, the MW was roughly around 204 kDa; The crystallinity reached more than 34.6 per cent and,alpha helix contents ranged from above 67.2％ to nearly 82.7%.

A serious part has more coupled descriptions. At 0.9 mol L-1 for 12 h, Mw fell to 82 kDa, PDI increased to 2.68, crystallinity decreased to 19.2%, helix retention fell to 39.4%, and β-1,3 retention decreased to 69.8%. SEC-MALS, XRD, Congo-red, and NMR-informed descriptors therefore jointly supported a depolymerized label with low ambiguity.

Figure 5 unifies these trends in the structure-and-constituent fields. Sint declined from 0.956 in the native control to 0.872 at 0.1 mol L-1 for 2 h, 0.626 at 0.5 mol L-1 for 6 h, and 0.354 at 0.9 mol L-1 for 12 h, corresponding to swelling-boundary, transition, and depolymerized regions.

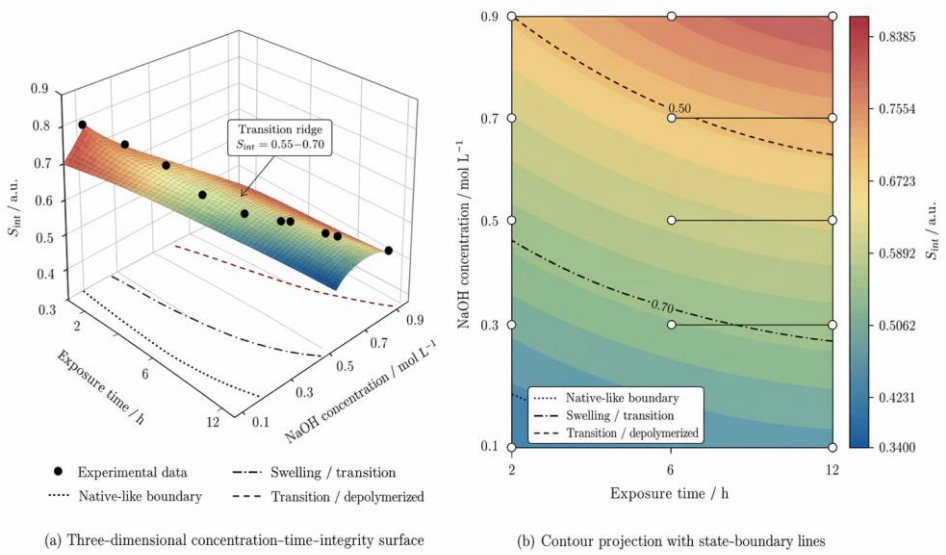

Figure 5. Evolution of three-dimensional structures of alkali-treatment-Euglena polysaccharide.

As shown in Figure 5, the structure distribution curve rather than plane. The reduction from 0.1 to 0.3 mol·L^-1 is relatively smooth after 2 hours; however, it increases significantly by 6 and 12 hours. Therefore, the relationship among concentration, time cannot be expressed by a simple addition. Figure 5 Projection panel also has a ridge for Sint between approximately 0.55 and 0.70. The first transformation zone is this hill. The samples in this area still have some of the beta-glucan fingerprint and molecular size distributions, but their crystallinity and conformations are already weakened. Since this region cannot be reliably determined by one instrument alone, it would not have been suitable for setting up an intelligent analysis system.

Empirical Descriptor Maps support a particular structure- evolution sequence. Mildly alkali-susceptible substances swell and lose some packing integrity but retain much of their molecular-size and β-1,3-linkage information. Moderate exposure degrades crystal order and retains triples; therefore, it shifts towards a mixture of transitions. Severe exposure includes conformational loss, extensive reduction of MW, large polydispersity, and decreased linkage retention. This Sequence is not determined by the model. Visible in the measured Descriptor field, and it will be used for checking if the fusion model has understood this pattern correctly.

As shown in Figure 5, time and concentration have varying degrees of contributions. Time increased from 2 to 12 hours, and reduced Sint dropped by 0.872%, but when it was raised from 0.1 to 0.9 mol·L^-1 at the same time point, it decreased from 0.801% to 0.354%. Therefore, the higher concentrations showed greater sensitivity; however, with increased exposure time over these levels, both exhibited comparable responses. Interaction Term Justifies adding the concentration-time product to the treatment embedding instead of using concentration alone.

3.2 Fusion performance, state topology, and prediction accuracy

Established after that were questions about whether the model could transform heterogeneous data into valid states and continuous properties of interest. Figure 6 presents the results of the state-topology and modalitiefficiency contributions; In addition, Table 3and Figures show a comprehensive assessment at the modellevel level. In addition, it compares a variety of single-modal and early-fusion approaches to determine the superiority of structured multimodal integration more clearly.

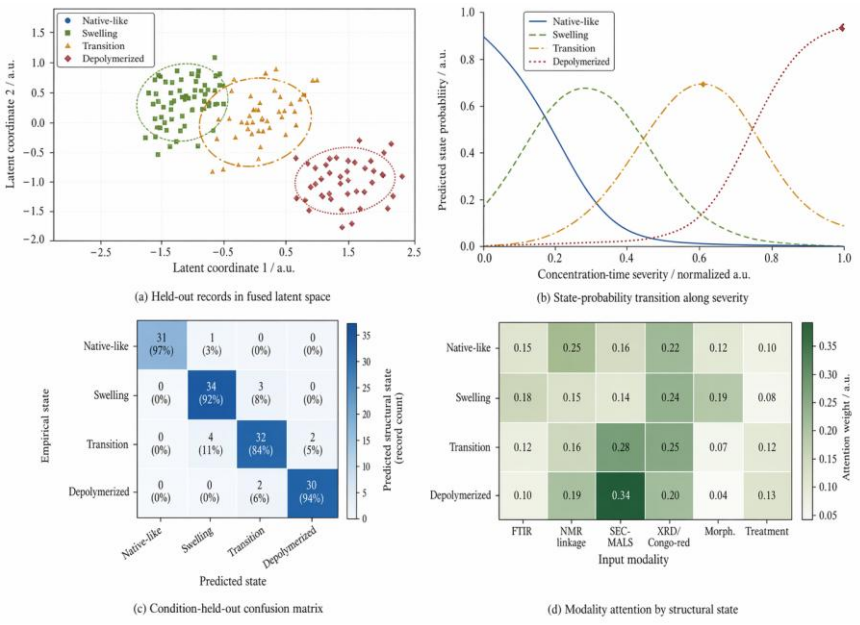

Figure 6. State Topology, Probability Transition, Confusion Matrix and Modality Attention for the proposed Fusion Model.

Figure 6(a) shows the latent projection of held-out records. Native-likematches occupy the high-impact area, depolymerization reactions belong to the severe-loss zone, swelling or transition regions have some overlapping in part. This kind of matching for measured Structural gradients: Swelling has a lower Order than transition; while transition contains higher Mw and conformation loss.

Figure 6(b) relates state probability to the concentration-time severity term. Native-like probability declines after the mild region; swelling peaks at low-to-moderate severity; transition peaks in the middle range; and depolymerized probability rises under high exposure. Ordered curves are consistent with the change of descriptors shown in Figures 4 and 5; thus, this model has learned a structural sequence rather than an unstructured four-class division.

Figure 6(c) shows the confusion matrix of condition-held-out data. The most stable native-like and depolymerised States are 31 and 30 correct classification. Swelling made 34 correct entries and entered three transitions incorrectly. Transition had three incorrect entries as swelling, and two wrongs were depolymerization. Errors mainly occurred between adjacent states, with no native-like/depolymerized reversal, preserving severity order for process screening.

As shown in Figure 6(a), this also reveals the error situation. The separate depolymerized and native-like records are caused by the difference of molecular weights, crystallinity, conformation and linkage. Both swelling and transition have decreased crystallinity, as well as changed their FTIR spectra. Separation breaks down as SEC-MALS, combined with XRD/Congo-red analysis, are employed.

As shown in Figure 6 (d), modalitieattentionbystructure states. Mainly native prediction based on NMR-based inferences and XRD/Congo-red evidences. Swelling increased morphology and conformation contributions. The transition-weighted SEC-MALS, and XRD/Congo-red showed the highest transitions, followed by depolymerization prediction was dominated by SEC-MALS, then conformation and linkage evidence. Treatment variables contributed more to transition and depolymerized states, where severity context carried stronger diagnostic value.

Table 3: Predictive Performance of Single-Modality, Early-Fusion and Proposed Models.

Model	Mw RMSE / kDa	S_int RMSE	Macro-F1	AUROC	ECE
FTIR-only	25.4	0.071	0.742	0.889	0.092
NMR-informed only	29.2	0.078	0.711	0.864	0.101
SEC-XRD baseline	18.7	0.052	0.794	0.918	0.071
Morphology-only	41.3	0.094	0.624	0.781	0.136
Early fusion	13.6	0.039	0.862	0.958	0.058
Proposed multimodal fusion	8.9	0.024	0.942	0.985	0.031

Figure 7(a) compares Mw prediction error. FTIR only: RMSE = 25.4 kDa; NMR only: RMSE = 29.2 kDa; SEC-XTDS: RMSE = 18.7 kDa; Morphology only: RMSE = 41.3 kDa; Early fusion: RMSE = 13.6 kDa; Proposed model: RMSE = 8.9 kDa. SEC-XRD was the best single-modality baseline, as it provides both size and order directly. The proposed model still reduced error by 34.6% relative to early fusion and by 52.4% relative to SEC-XRD. The enhancement stems from letting the model adaptively assign a modality-weight based on structure in place rather than considering all feature blocks equally dependable.

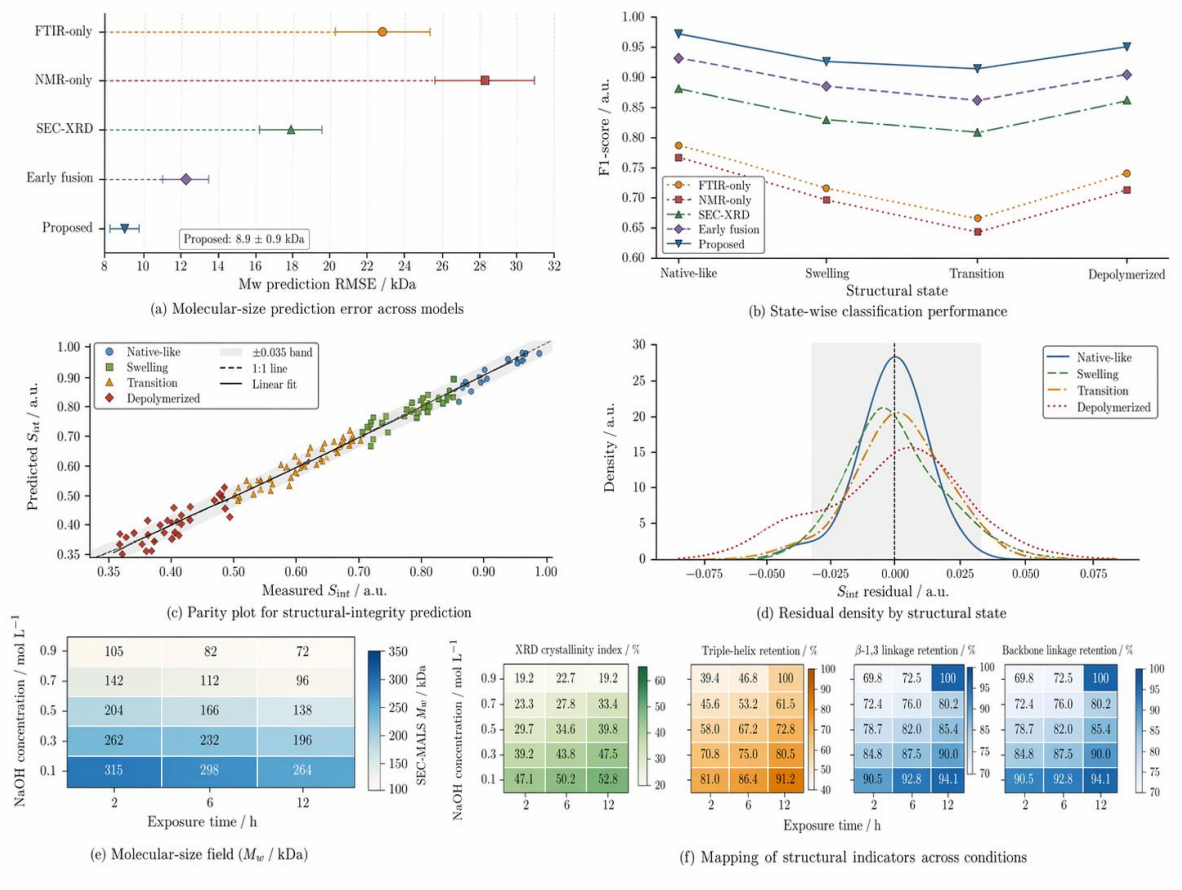

Figure 7: Prediction accuracy and residual analysis of the multimodal fusion approach.

Table 3: None of the individual modalities can capture all classes simultaneously. FTIR-only screening produced a macro-F1 of 0.742, which is useful for rapid sorting but not final state assignment. NMR-informed descriptors had high chemical specificity but lower coverage and produced a macro-F1 of 0.711. SEC-XRD reached 0.794 because it had molecular-sized and ordered features; however, it could not capture the whole swelling-transition boundary. Morphology-only classification reached 0.624; therefore, particles alone cannot be used to judge back-bone's integrity.

There is a notable discrepancy in the results of early fusion and this method. Early fusion used the same descriptor pool, but its macro-F1 was 0.862 and Mw RMSE was 13.6 kDa. The results of this improvement reached 0.942 and 8.9 kDa, respectively. Modalities are treated as structured evidence blocks, and the treatment embeddings, masks, and consistency constraints have different origins. A concatenated vector learns correlations but cannot report that particular measurement family has influenced the state decision or whether confidence should vary based on having access to certain data points.

Figures (a)(b): State Classification Comparison. The proposed model reached a macro-F1 of 0.942 and an AUROC of 0.985. Early fusion reached a macro-F1 of 0.862 and an AUROC of 0.958. The best single-modality baseline, SEC-XRD, achieved a macro-F1 score of 0.794. The biggest change was in the transition class, and the model had less confusion about swelling. The corresponding chemical explanation is as follows: Transition samples need to provide proof of molecular size distribution, conformation, and treatment-induced change; Swelling can only be measured through morphological changes and non-strictly chain-size loss-related descriptors.

Figure 7(c) shows the parity diagram of S_int prediction. Most of the data are distributed relatively closely along the main diagonal axis; The deviations occur at some other locations

near S_int=0.55~0.70. The total S_int RMSE is 0.024. The former is smaller than the empirical difference for the important treatment zones. S_int reduced from 0.872 at 0.1 mol·L-1 for 2 hours to 0.626 at 0.5 mol·L-1 after 6 hours; There is a separation of 0.246. Thus, the model error is sufficiently small for differentiation between mild swelling and transition. The adjacent transition records are still relatively close, so they need to be interpreted with uncertainty instead of a single round-off grade.

Figure 7(d) shows the residual distribution. The residuals are quite small, typically less than 0.035 from zero. Tail length increased in response to greater severity and a stronger effect of exposure to strong alkali. Severe treatment generates large amounts of particles with uneven surfaces and wide distributions; thus, only one integrity score can be assigned. A residual plot can serve to make the model function as an auxiliary tool for decisions; only high uncertainty data need verification.

Figure 7(d)'s residual pattern is also consistent with the empirical labels. The errors were lowest for the native-like and mild-swelling areas; Descriptor Agreement was high. Errors widened near transition and severe depolymerization. The basic material is actually combined near the edge area; In the severe part, Fragmented heterogeneity and a wider PDI increase Diversity. Therefore, there is a chemical nature in the model error and does not appear randomly throughout the concentration-time plot.

3.3 Ablation, missing-modality robustness, calibration, and case interpretation

Finally, this part verifies that the proposed system is still valid if any component or measurement block is removed individually. Because the routine laboratory does not necessarily have a comprehensive modality for each batch. Figures 8-10 evaluate the model ablation effect and test cases for missing modality; Figure 9 assesses calibration performance and operation behaviour under abnormal conditions.

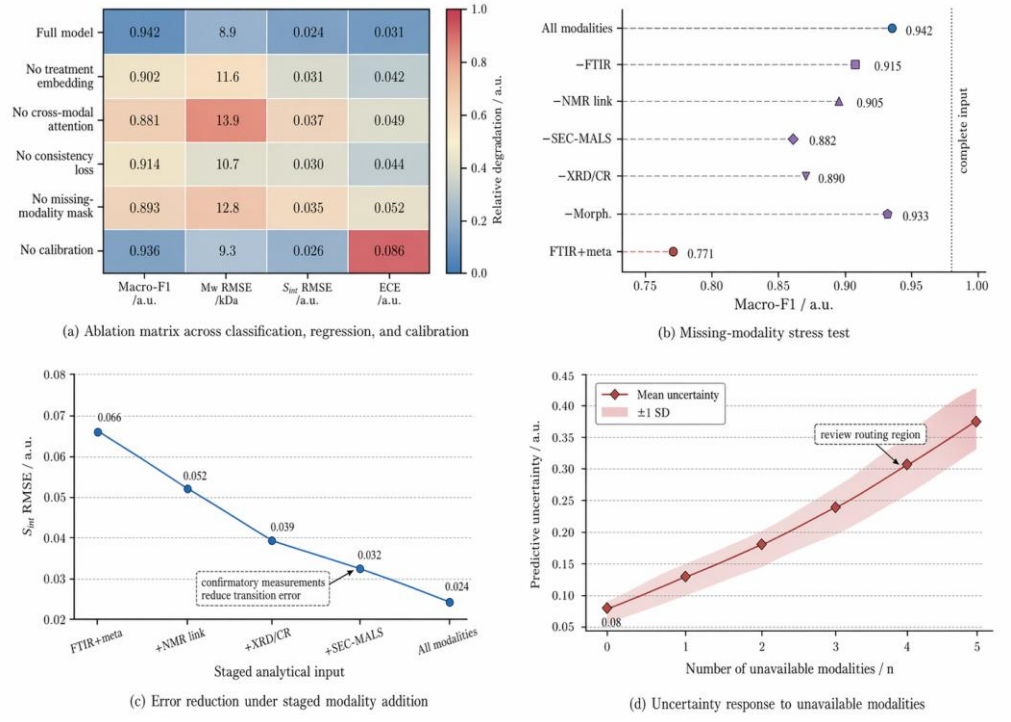

Figure 8: Ablation and missing-modality robustness of the multimodal fusion system.

Figure 8(a) is the ablated results. Reducing the removal of treatment embedding reduced macro-F1 to 0.942 and increased Mw RMSE by 8.9% to 11.6 kDa. Without removing the cross-modal attention term, the macro-F1 was further reduced to 0.881 and the Mw RMSE increased to 13.9kDa. By eliminating the structural-constancy loss, macro-F1 fell to 0.914, and chemically incompatible continuous output increases; although it had a relatively small impact on classification performance compared with removing attention. Removing the missing-modality mask reduced macro-F1 to 0.893. After removing calibration, it showed about zero-point-zero-six-macro-f1-score gain at most or below; The values oscillated from negative three-eights to positive twenty-five-nineties-two-hundreds-one.

Ablation Results show which components of the System can achieve empirical validity to some extent. Removing attention decreased the classification loss most significantly and reduced the macro-F1 score to 0.881. Removing the treatment embedding decreased the macro-F1 score to 0.902; therefore, only measuring descriptors are insufficiently encoding exposure environment. Without adding the consistency term, there was less impact on macro-F1; However, Chemically inconsistent outputs increased significantly. It is necessary to make this difference; a model may have correctly classified labels but give continuous outputs difficult to understand.

Lack of multiplicity can thus be quantified concretely. SEC-MALS removal caused the largest single-modality drop, reducing macro-F1 to 0.884 and increasing Sint RMSE. XRD/Congo-red removal decreased its efficiency due to changes in structure and order arrangement at the transition boundary. The NMR-derived features helped establish a connection but did not harm predictions as much when SEC-MALS or conformation information was available. Morphology exhibited the lowest degree of performance reduction; thus, it remained necessary for understanding physical swelling and fragmentation.

Figure 8(b) shows the missing-modality test. All modes are enabled; Macro-F1 is 0.942. Removing FTIR reduced macro-F1 to 0.918. Removing NMR-informed descriptors reduced it to 0.903. Removing SEC-MALS reduced it to 0.884, the largest single-modality drop. Removing XRD/Congo-red reduced it to 0.891. Removing morphology reduced it to 0.928. These values show that SEC-MALS and conformation descriptors are most important for separating transition and depolymerized states, while morphology mainly improves swelling interpretation. The FTIR-only plus metadata setting reached 0.768, which is useful for preliminary screening but insufficient for final structural-state assignment.

Figure 8(c) reports S_int error under masked inputs. The all-modality set has an error of 0.024. Removing SEC-MALS increased the RMSE to 0.041, and removing XRD/Congo-red increased this value to 0.039. FTIR+metadata alone increased RMSE to 0.066. SEC-MALS added 0.044 to the original score, then XOR-D was applied to reduce this figure to 0.032. These results support a staged laboratory workflow: use FTIR and treatment logs for high-throughput screening, then add SEC-MALS and conformation measurements for records that fall near the swelling-transition boundary.

Figure 8(d) shows that predictive uncertainty increased as more modalities were unavailable. Mean uncertainty: From 0.08 in the full condition to 0.38 when no modes are available. Such an adjustment must be made for both the absence and presence of data to alter the assessment of labels accordingly. The model therefore supports a review rule. If the state probability is low or if there is uncertainty, then it will route this record for confirmation; otherwise, it assigns a final process judgment.

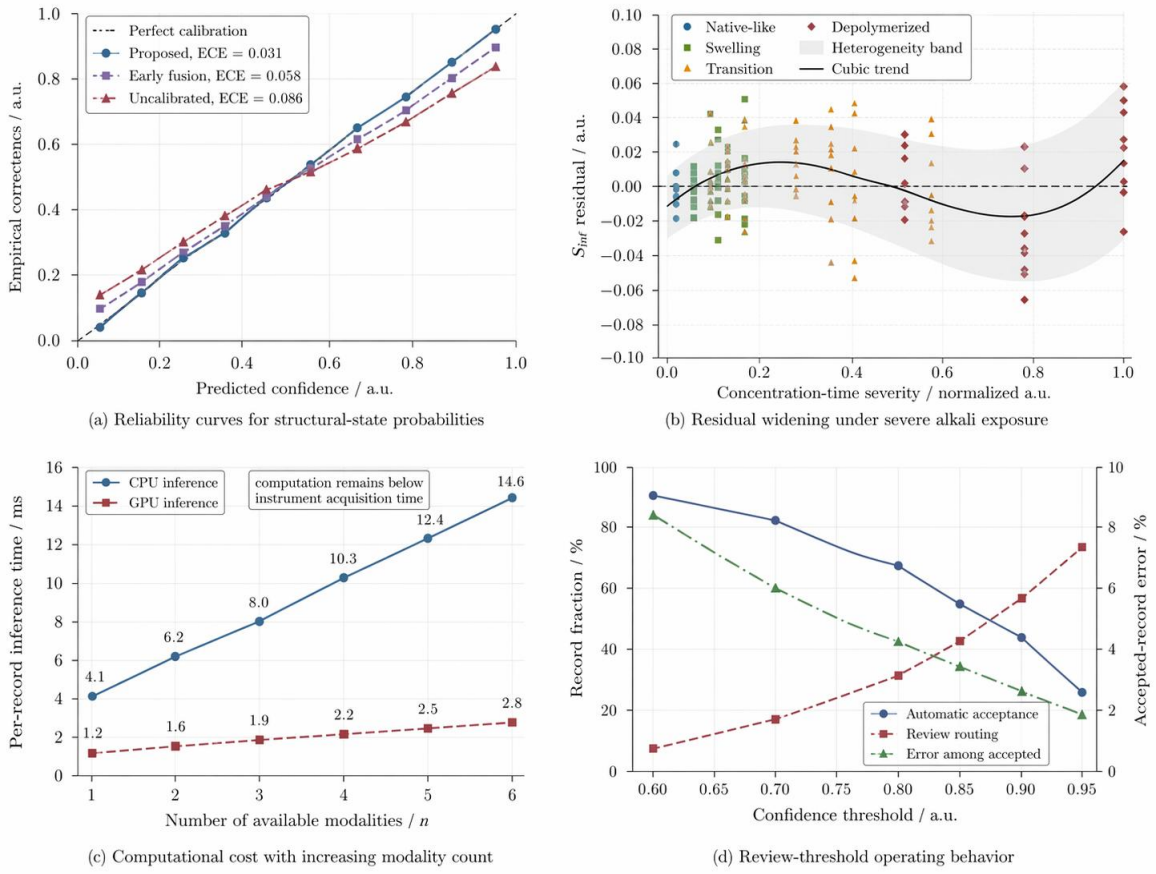

Figure 9: Calibration, Residual Severity, Computational Efficiency and Review-Threshold Behavior.

Figure 9(a) shows the reliability curves. The calibrated model is relatively close to a diagonal distribution, and its expected calibration error is 0.031. Early fusion had an ECE of 0.058, and the uncalibrated ablation had an ECE of 0.086. In particular calibration of the transition sample. A 0.55 transition probability needs to be reviewed, and a 0.90 depolymerisation probability supports rejecting or treating seriously. Calibration must first take place to apply the probability estimates operationally.

Figure 9(b) plots S_int residuals against the concentration-time severity term. Residuals are smaller at moderate values, but higher than this range. Severe ones had resididuals within the range of ±0.04. The above distribution shows real sample heterogeneity; high-alkali-concentration-long-exposure samples produced wider polydispersity artefacts compared to other types of samples. The residual model also shows the location for next-time experiment. Additional SEC-MALS replications and direct linkages have greater value in the severe and transitional areas compared to the native-like corners.

See Figure 9: Model output and laboratory operations. Calibration narrowed the difference between predicted confidence and empirical accuracy, and by calculating when a certain number of records should be judged as positive or negatively reviewed, respectively. It does not set an all-encompassing judgment standard. It offers a selectable working state. A product line focusing on preserving the structure can set a lower confidence level and send more test results to confirmatory SEC-MALS or XRD/Congo-red analyses. Screening campaigns are set at a relatively low level to reduce expenditure and accept an uncertain degree.

As shown in Figures 10(a)-(c), the case-specific outcomes are easy to understand. The original case kept high descriptors and was categorised as indigenous with a confidence of 0.95.

A weak example was observed to have a reduced degree of crystals and forms but retained substantial molecular structure stability; consequently, its probability index for polymers swelling reached 0.68. The moderate case was at the probability of 0.70 because Mw, helix retention, and crystallinity were all reduced but linkage retention could still be detected. Severe cases had the highest depolymerisation rate, with the greatest degree of structural loss in all Descriptor Blocks.

See Figure 9(c): inferences cost. The change after each inference increased by 20% as the number of combination types exceeded one through an overall examination. Within this limit on the GPU: about 1.2-2.8 milliseconds. Relative to the cost of instrument purchase and experiment settings, etc. Therefore, the limitation of characterisation throughput exists rather than an issue with computation. Figure 9(d) shows review-time behaviour. At a confidence level of 0.70, 82 per cent of the records were classified as accepted immediately; Additionally, due to multi-state probability, some cases may have been identified by either category (accepted or reviewed). By setting the threshold at 0.85, reducing automatic acceptance to 58%, increasing review routing to 70%. An adjustable Threshold can be chosen by the laboratory for strict or permissive Screening Policies.

The following represents the example of representative-case interpretation: Selected four sets of data: The native control was the untreated group; Mildly treated at 0.1 mol/L for 2 hours, moderately treated at 0.5 mol/L for 6 hours, severely treated at 0.9 mol/L for 12 hours. The chosen examples include both paths of structural evolution and demonstrate that the model employs cross-modal evidence.

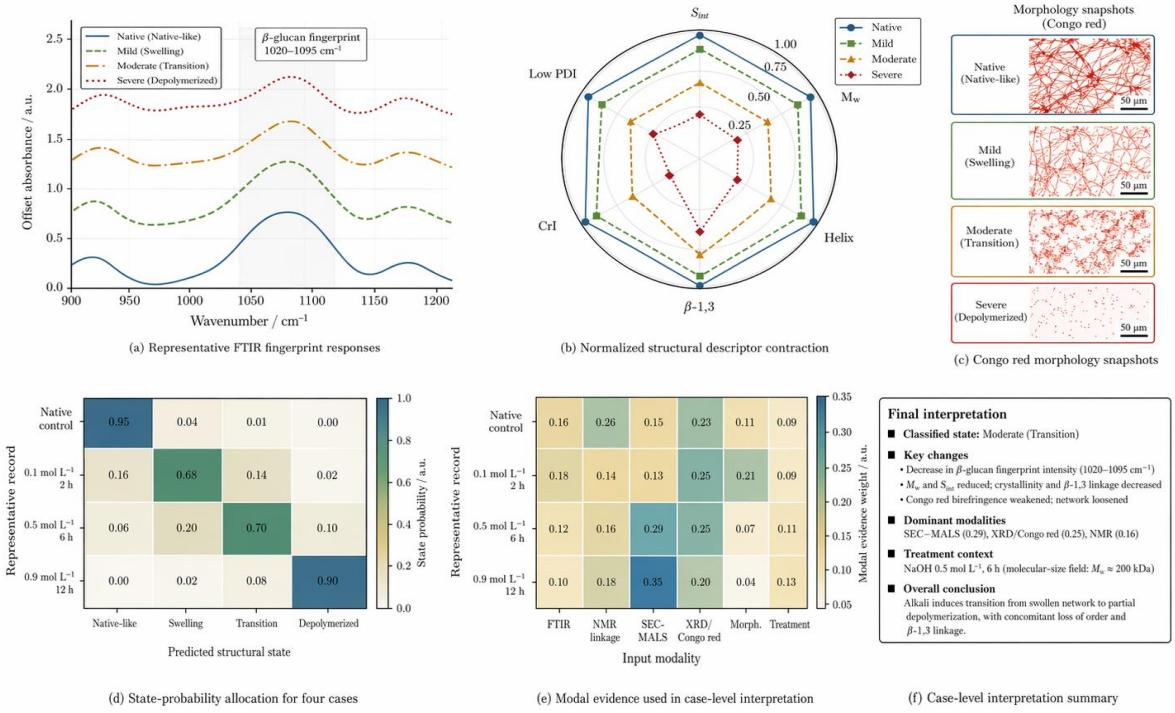

Figure 10: Example representation of spectrum-linking with descriptor, state probability and modality evidence.

Figure 10(a) shows the FTIR fingerprint curves. The original and moderate cases still had a prominent beta-glucan-shaped spectrum. The intermediate case had an insufficient fingerprint region and a more pronounced disorder-based reaction. The severe case showed the largest spectral redistribution. Figure 10(b) shows the descriptor radar. The original data were close to the periphery of S_int, Mw, helix retention, beta-1,3 retention, crystallinity, etc. The mild case

mainly contracted in crystallinity and conformation. The moderate case contracted across Mw-helix-crystallinity, and the severe cases only showed contractions for all descriptor systems.

Figure 10(C) presents state Probabilities. The native case had an inherent probability of 0.95. Mildness had a swelled-up occurrence likelihood of 0.68 and a converted likelihood of 0.14. The moderately severe case had a transition probability of 0.70 and a depolymerised proportion of 0.10; The serious case had a depolymerisation probability of 0.90. Figure 10(d) reports modal evidence. The medium-case received more evidence of the SEC-MALs- and X-RD-Congo-red-based approaches; The severe case was identified most effectively by using the medium case. The assignment of this evidence aligns with the chemistry behind alkali-triggered structural degradation.

Empirical data support treating the system as the decision-making Layer Laboratory. It cannot replace chemical characterisation; it can predict at most within the reliability bounds of the measured modes and calibration domains. It retains an agreement in terms of the evidence. It identifies mild edema conditions; distinguishes between transitional records and serious decomposition; reports the lack of uncertain modalities; gives cases' evidences for experts to refer to. For alkali-processed Euglena polysaccharides, it transforms a series of independent instrument responses into an evolutive path chart for guiding batches of screening and experimental design.

At the application end, a staged explanation of this form is supported by recent research on paramylon productivity, biological relevance, derivatisation and solvent processing [21-25]. Higher paramylon output and broader product use increase the cost of misclassifying a treated material. A quick judgment that the transition sample passes may send a structureally weak batch for further processing incorrectly. Restrictive Type Rejects All Swollen Samples; Therefore Good Materials May be Missed. Calibrated Fusion can be used to distinguish between these two situations, reporting that more evidence is required when necessary.

Domain scope of the primary empirical issue. The data set contains only one Euglena materialsource; there was onlyone treatmenttemperature and a calculated NaOH-concentration-timematrix. The acquired threshold values should not be directly applied to other strains, dry histories or alkaline solvents. The model architecture can be reused, but the calibration and state-boundary values need local data. The future experiment will add more temperature, solvents and functions in the tests to link structural states with viscosities, dispersions, immunological responses or formulation behaviours.

4 Conclusion

A novel intelligent multi-modal analysis System to study the Structural Evolution of alkali treated Euglena polysaccharide based on this research. The work adopted a control-NaOH concentration-times Matrix, multiple-mode Structural characterisation, recorded-level Data organisation, and Condition-hold-out Model verification. Therefore, the resultant system integrates information of treatments applied, spectral signals; molecular-weight distribution; crystallinity degree, etc., into a single understandable result.

Stays within the testable experimental domain for the interpretations. The reported thresholds and performance values are valid under the conditions of a NaOH concentration-time matrix, 45°C treatment condition, modality selection and experimental setup described in this work. They offer a verifiable empirical example of this data set and a generalisable analytical infrastructure for other datasets once the state-boundaries have been re-established using local observations.

(1) The first experimentally derived descriptive Map exhibited a stepwise alkaline reaction. Alkali-exposed mild retention of many Mw, β-1,3-linkage information but reduced the

content of crystals and conformers. About 0.55 to 0.7 moderate exposure zones were created approximately. Severe exposure decreased from 82 kDa to 0.354 under 0.9 mol/L for 12 hours, which suggested a certain degree of depolymerisation hazard.Mw

(2) The proposed Fusion Model outperformed the single-modal and early-ensemble baselines. Mw RMSE was 8.9 kDa, S_{int} RMSE was 0.024, macro-F1 score was 0.942, AUC was 0.985, and the expected calibration error was 0.031. Ablation testing found that masked cross-modal attention, Treatment Embedding, Consistency Loss, and Calibration separately enhanced the model's accuracy, Chemical Coherence, or Decisive Reliability.

(3) The system has good compatibility with staged characterisation. FTIR and treatment logs can provide initial screening; SEC-MALS and XRD/Congo-red measurements need to be taken as priorities for transitions and high-uncertainty data. Mainly the problem of calibration range. These values are for the examined Euglena samples under the test conditions and data acquisition methods. Future research could expand the training dataset beyond single Strain-Extraction-Rout-Electrode configurations by including multiple variations; thus linking Structural-State predictions with Application-Specific Product Properties.

At present, the System is an assessed layer that supports calibration in applications. To alleviate the routine interpretation workload and focus on confirming critical items, but these must be linked to experimental descriptions and local qualification limits. The Boundary is necessary to maintain the empirical nature of this study.

Funding

This work was supported by National Natural Science Foundation of China (No.22278182) and the Jiangsu Province “Collaborative Innovation Center of Food Safety and Quality Control” industry development program.

About the Author

Yingtong Sui is the first author of this paper. She is currently a Master’s candidate majoring in Food Science at the School of Food Science and Technology, Jiangnan University. Her research interests focus on food science and related fields.

References

[1] Zhang, K., Wan, M., Bai, W., et al. (2023). A novel method for extraction of paramylon from Euglena gracilis for industrial production. Algal Research, 71, 103058.

[2] Wang, Q., Alam, M. A., Wang, J., et al. (2025). An innovative method for the extraction of paramylon (beta-1,3-glucan) from Euglena gracilis using alkaline deep eutectic solvent and functional property analysis. Biomass Conversion and Biorefinery, 15, 12739-12752.

[3] Wu, J., Yu, X., Wei, L., et al. (2025). Paramylon biorefinery from Euglena gracilis via recyclable aqueous two-phase system: A sustainable platform for high-content beta-1,3-glucan production. Carbohydrate Polymers, 370, 124365.

[4] Kim, K., Kang, J., Seo, H., et al. (2024). A novel screening strategy utilizing aniline blue and calcofluor white to develop paramylon-rich mutants of Euglena gracilis. Algal Research, 78, 103408.

[5] Huang, X., Wen, Y., Chen, Y., et al. (2023). Structural characterization of Euglena gracilis polysaccharide and its in vitro hypoglycemic effects by alleviating insulin resistance. International Journal of Biological Macromolecules, 236, 123984.

[6] Gao, L., Zhao, X., Meng, L., et al. (2022). The characterization and functional properties of Euglena gracilis paramylon treated with different methods. Evidence-Based Complementary and Alternative Medicine, 2022, 7811014.

[7] Hong, T., Yin, J. Y., Nie, S. P., et al. (2021). Applications of infrared spectroscopy in polysaccharide structural analysis: Progress, challenge and perspective. Food Chemistry: X, 12, 100168.

[8] Guo, X., Kang, J., Xu, Z., et al. (2021). Triple-helix polysaccharides: Formation mechanisms and analytical methods. Carbohydrate Polymers, 262, 117962.

[9] Liu, J. J., Chen, S. K., Wang, X., et al. (2024). Changes of the physicochemical properties and structural characteristics of alkali-extracted polysaccharides from Agrocybe cylindracea across the growth process. Journal of Agricultural and Food Chemistry, 72(22), 12810-12821.

[10] Lin, J., Deng, J., Huang, Z., et al. (2023). Physicochemical and structural characterization of alkali-treated biopolymer sphingan WL gum from marine Sphingomonas sp. WG. ACS Omega, 8(7), 7163-7171.

[11] Guo, M., Wang, K., Lin, H., et al. (2024). Spectral data fusion in nondestructive detection of food products: Strategies, recent applications, and future perspectives. Comprehensive Reviews in Food Science and Food Safety, 23(1), e13301.

[12] Strani, L., Durante, C., Cocchi, M., et al. (2024). Data fusion strategies for the integration of diverse non-destructive spectral sensors (NDSS) in food analysis. TrAC Trends in Analytical Chemistry, 180, 117957.

[13] Hanzelik, P. P., Gergely, S., Abonyi, J., et al. (2025). Data fusion of spectroscopic data for enhancing machine learning model performance. Digital Chemical Engineering, 17, 100271.

[14] Xiao, Y., Li, Y., Cui, G., et al. (2025). A systematic review of multimodal fusion technologies for food quality and safety assessment: Recent advances and future trends. Trends in Food Science & Technology, 164, 105277.

[15] Song, H., Zhou, X., Chen, C., et al. (2024). Multimodal separation and cross fusion network based on Raman spectroscopy and FTIR spectroscopy for diagnosis of thyroid malignant tumor metastasis. Scientific Reports, 14, 29125.

[16] Vaswani, A., Shazeer, N., Parmar, N., et al. (2017). Attention is all you need. In Advances in Neural Information Processing Systems (Vol. 30, pp. 5998-6008).

[17] Guo, C., Pleiss, G., Sun, Y., et al. (2017). On calibration of modern neural networks. In Proceedings of Machine Learning Research (Vol. 70, pp. 1321-1330).

[18] Lundberg, S. M., & Lee, S. I. (2017). A unified approach to interpreting model predictions.

In Advances in Neural Information Processing Systems (Vol. 30, pp. 4765-4774).

[19] Kingma, D. P., & Ba, J. (2015). Adam: A method for stochastic optimization. In International Conference on Learning Representations.

[20] McInnes, L., Healy, J., & Melville, J. (2018). UMAP: Uniform manifold approximation and projection for dimension reduction. arXiv, 1802.03426.

[21] Yan, X., Xu, H., Yang, Z., et al. (2025). Synergistic enhancement of paramylon production in edible microalga Euglena gracilis via ethanol-guaiacol co-regulation. Foods, 14(14), 2457.

[22] Rubiyatno, Mori, K., Toyama, T., et al. (2021). Isolation and characterization of Euglena gracilis-associated bacteria capable of promoting growth and paramylon production. Microorganisms, 9(7), 1496.

[23] Ryan, C., Cao, S., Sekiguchi, M., et al. (2023). Euglena gracilis-derived beta-glucan paramylon entrains the peripheral circadian clocks in mice. Frontiers in Nutrition, 10, 1113118.

[24] Daglio, Y., Rodriguez, M. C., Prado, H. J., et al. (2019). Paramylon and synthesis of its ionic derivatives: Applications as pharmaceutical tablet disintegrants and as colloid flocculants. Carbohydrate Research, 484, 107779.

[25] Feuzing, F., Mbakidi, J. P., Lazar, F., et al. (2023). Biobased ionic liquids as solvents of paramylon. Journal of Molecular Liquids, 370, 120983.